Experimental and Computational Study of the Aerodynamic Performance of a Formula Student Vehicle

Diogo Casaleiro Vitoriano dos Santos
diogo.santos.22@tecnico.ulisboa.pt

Instituto Superior Técnico, Universidade de Lisboa, Portugal

December 2025

Abstract

This work presents the aerodynamic study of the FST14, the latest Formula Student prototype developed by FST Lisboa, focusing on its side elements. The study aimed not only to improve the vehicle's aerodynamic performance but also to evaluate and consolidate the numerical methodology used in the team's design process. A comprehensive computational fluid dynamics (CFD) framework was established, including mesh convergence studies, numerical error estimation, and a systematic assessment of the isolated effects of blockage, scaling, wheel and ground motion, and ground clearance variations on the numerical results. The analysis focused on three side element configurations to identify the most effective design in terms of aerodynamic efficiency and overall contribution to vehicle performance. To evaluate the reliability of the numerical predictions, a 1:3 scale model of the FST14 was designed, manufactured, and tested in the closed circuit wind tunnel at LNEC. The aerodynamic force balance was recalibrated, enabling measurement of global forces and moments together with surface static pressures and flow visualization using wool tufts. Despite measurement uncertainties, the experimental results demonstrated consistent aerodynamic trends and agreement with the numerical data, reinforcing confidence in the CFD methodology. Finally, the numerical framework was extended to replicate on-track conditions, enabling assessment of aerodynamic behavior beyond wind tunnel constraints. The modified boundary conditions altered the performance hierarchy among configurations, affecting downforce, drag, and side element contribution. These findings redefined the observed aerodynamic trends and guided the selection of the optimal configuration for integration into the FST14 prototype under real-world conditions.

Keywords: Aerodynamic Design, Experimental Validation, Computational Fluid Dynamics, Wind Tunnel Testing, Race Car Aerodynamics, Formula Student.

1. Introduction

Ground effect aerodynamics plays a decisive role in the performance of open-wheel racing cars, where the generation of downforce without excessive drag directly influences cornering capability and overall lap time [1–3]. In Formula Student (FS), where vehicles operate at relatively low Reynolds numbers and within strict design envelopes [4], achieving this aerodynamic efficiency is particularly demanding. The flow around open-wheel cars is characterized by intense three-dimensional flow behavior, large wake regions, and strong vortex interactions, making it more complex to simulate accurately through Computational Fluid Dynamics (CFD) solely [5, 6]. Consequently, experimental testing remains indispensable to evaluate numerical methodologies, ensuring reliable simulated results under realistic operating conditions [7, 8].

The side aerodynamic elements of the latest Formula Student Técnico (FST) Lisboa prototype, the FST14, were selected for detailed study due to their significant contribution to downforce generation, as shown in Figure 1, mainly through ground effect. Their position allows them to exploit low pressure regions efficiently while controlling the interaction between the front wheel wake and the downstream flow. Previous FST Lisboa studies have already highlighted the importance of integrating experimental testing within the design process. The work by Pacheco [9] demonstrated that CFD could indeed capture the global aerodynamic trends observed experimentally, while also highlighting the need to correct the numerical simulations replicating the wind tunnel environment for Reynolds scaling and boundary condition simplifications to enhance the comparison of results under on-track conditions. Similarly, Afonso [10] and Morgado [11] emphasized the necessity of coupling CFD and Experimental Fluid Dynamics (EFD) for meaningful aerodynamic design. However, none of these studies provided a quantitative assessment of how confinement, ground motion, ride height, or wheel rotation differences individually affect the aerodynamic performance in scaled car model testing.

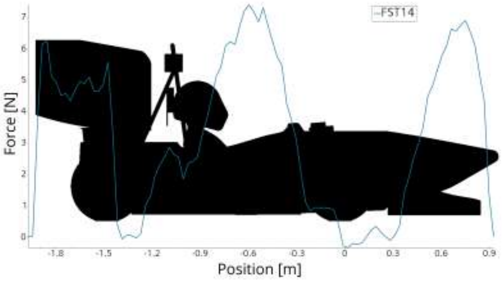

Figure 1: FST14's downforce distribution.

The present work addresses this gap by establishing a systematic correlation between CFD and wind tunnel measurements to quantify the aerodynamic deviations induced by key boundary condition differences. A comprehensive numerical framework was developed and verified through mesh convergence and numerical error analyses, followed by wind tunnel testing with a 1:3 scale complete car FST14 model at the closed circuit facility of the Laboratório Nacional de Engenharia Civil (LNEC). The experimental setup employed a six-component aerodynamic force balance capable of measuring overall aerodynamic forces and moments [12]. Additionally, surface pressures simultaneously with wool tuft visualization were also carried out enabling a reliable and complete comparison with CFD simulations.

The numerical setup was used to reproduce a sequence of progressively more realistic on-track conditions, isolating the effects of Reynolds number, ride height, blockage, and ground and wheel motion. The resulting analysis provides a quantitative understanding of how confined flow testing differs from open flow behavior, demonstrating that conclusions drawn solely from wind tunnel tests under such conditions must be carefully interpreted, as they do not fully represent the behavior observed under real-world operating conditions.

2. Race Car Aerodynamics

The generation of downforce is essential to maximize cornering capability and overall grip, while drag must be minimized to preserve straight line performance [5]. In ground effect configurations, the proximity between the car floor and the ground surface accelerates the flow beneath the vehicle, further reducing static pressure and creating an additional suction force [2, 13]. The magnitude of this effect depends on parameters such as ground clearance, expansion angle, and underfloor curvature, which collectively determine the pressure recovery capacity and the stability of the flow [14]. Excessive expansion or abrupt curvature may cause boundary layer separation and a rapid loss of suction, thereby reducing both aerodynamic efficiency and stability [7].

The aerodynamic devices of a Formula Student car are designed to exploit these principles within a compact and tightly integrated system. The front wing manages the airflow entering the underfloor and downstream components, influencing both front downforce and the efficiency of the subsequent elements. The side elements, particularly their main wing, form the core of the low pressure system, where the airfoil section accelerates the flow beneath the car and recovers static pressure at the exit. The rear wing operates in the wake of the upstream components and at a higher position, contributing one of the largest portions of the total downforce while defining the overall aerodynamic balance [5] (see Figure 1). Endplates, vortex generators, and Gurney flaps are some of the auxiliary appendages that complement the primary aerodynamic components by guiding tip vortices and enhancing suction.

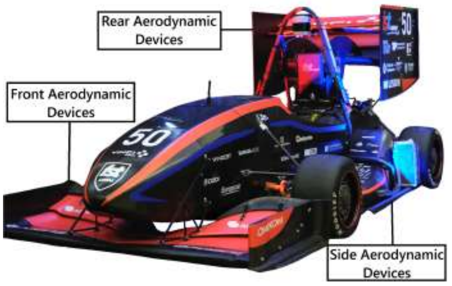

Figure 2: FST14's main aerodynamic devices.

3. Numerical Aerodynamic Model

The numerical analyses were carried out using a steady state Reynolds Averaged Navier–Stokes (RANS)[15] solver in *STAR-CCM+*®, aiming to establish a verified computational methodology capable of simulating both wind tunnel (WT) and on-track aerodynamic conditions. The computational domain, initially defined as a closed rectangular volume matching the LNEC test section and inlet-to-model distances, was later expanded to represent open-flow conditions, as illustrated in Figure 3. Boundary conditions reproduced the experimental setup with a uniform velocity inlet, a pressure outlet, static lateral and upper walls, and a steady ground plane. Due to the geometric and flow symmetry, only half of the domain was modeled. For on-track simulations, these were progressively modified to include a moving ground, rotating wheels, and enlarged far-field boundaries to minimize blockage effects.

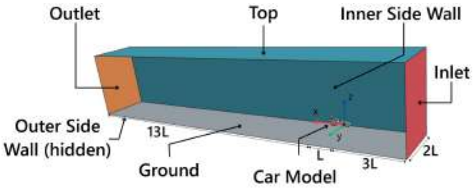

Figure 3: On-track simulation domain.

Polyhedral cells were employed to ensure numerical robustness and accuracy over complex geometries, complemented by prism layers near selected walls to resolve the boundary layer down to the viscous sublayer, maintaining $y^+ < 1$. Local mesh refinement regions were defined around the wheels, wings, and side elements to capture strong pressure gradients and vortex structures more accurately, as illustrated in Figure 4. The k–ω SST turbulence model [16] was selected for its demonstrated capability to handle near wall adverse pressure gradients and flow separation phenomena characteristic of ground effect race car aerodynamics. Convergence of the solver was evaluated based on the decay of normalized residuals below 10^{-4} and the stabilization of the integrated aerodynamic coefficients.

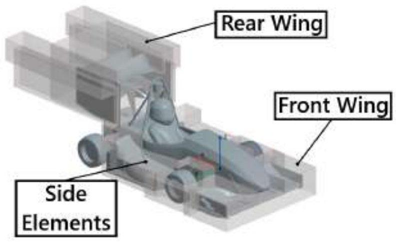

Figure 4: Refinement boxes around the aerodynamic package.

Verification of the numerical setup was conducted through a systematic mesh convergence study following the methodology of Eça and Hoekstra [17]. Five geometrically similar meshes were generated using a constant refinement ratio, Ri, to ensure grid similarity across different resolutions. Round-off errors were considered negligible due to the use of double precision. Iterative errors were estimated from the variation of aerodynamic coefficients between successive iterations of each simulation [18], while discretization errors and the observed order of accuracy were quantified using Richardson extrapolation [17]. The discretization component was identified as the primary source of numerical uncertainty.

The evolution of the lift and drag coefficients with mesh refinement, presented in Figure 5, exhibited monotonic convergence with a consistent decrease in numerical uncertainty. The uncertainties presented were calculated conservatively, as indicated by the high safety factors, primarily due to the data scatter observed in the results, which was expected given the geometric complexity of the problem. The third level of mesh refinement level, shown in Figure 6, provided an optimal compromise between computational cost and accuracy and was adopted for all subsequent simulations.

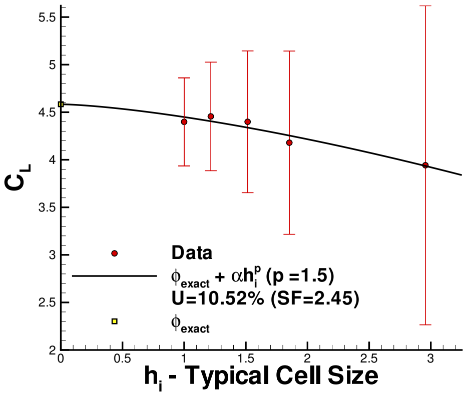

(a) Lift coefficient.

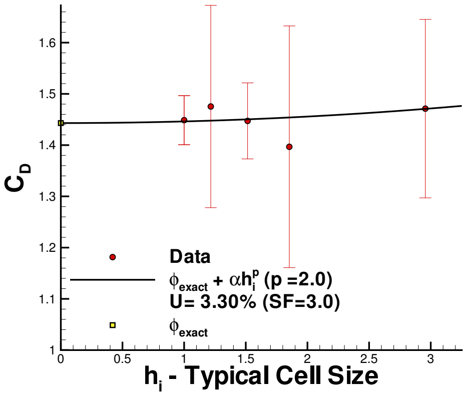

(b) Drag coefficient.

Figure 5: Estimation of the discretization error.

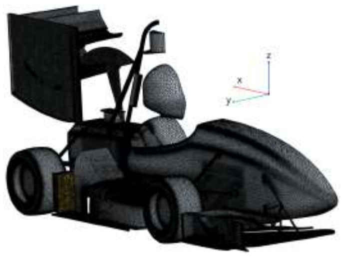

Figure 6: Numerical mesh on the car surface.

The estimated numerical uncertainties are a consequence from the estimated discretization errors of 4.29% and 1.1% for the lift and drag coefficients, respectively. This verification process ensured that the aerodynamic trends analyzed in the subsequent stages of this work could be attributed to physical effects, such as boundary condition variations and geometric modifications, rather than numerical uncertainty.

4. Wind Tunnel Experimental Setup

The experimental setup was developed to enable reliable aerodynamic measurements during the wind tunnel testing. The 1:3 scale model of the FST14 was mounted on a six-component aerodynamic force balance [12], which underwent mechanical repairs and a complete recalibration procedure to ensure measurement accuracy and reliability across all axes.

The force balance calibration was performed using a custom-built apparatus [19] capable of applying known forces and moments through a cable and pulley system designed to replicate the expected load ranges. The resulting strain gauge data were processed using a weighted least-squares method [12] to derive the calibration matrix relating sensor outputs to the resultant aerodynamic loads acting on the model. A total of 221 load cases were applied (see example in Figure 7), encompassing the full range of aerodynamic forces and moments anticipated during testing and enabling the assessment of cross-axis sensitivity and potential non-linear coupling between measurement channels.

Figure 7: Pure vertical load case for calibration.

The experimental campaign was carried out in the LNEC closed circuit aeronautical wind tunnel, shown in Figure 8, whose 1.2 × 1.0 m test section and adjustable fan drive provided stable, controllable, and uniform free stream conditions. Flow uniformity and turbulence intensity, TI, were certified through institutional characterization giving $TI < 1\%$. Data acquisition was performed using *National Instruments*® *NI* 9237 modules for strain-gauge signal acquisition and a *Pressure Systems*® ESP-64HD pressure scanner for surface pressure measurements. Sampling frequencies and averaging procedures were optimized to minimize electronic noise and ensure signal stability

The car model was mounted through an attachment system that ensured pitch, yaw, and roll alignment relative to the free stream, maintaining geometric repeatability across all configurations. The test matrix included aerodynamic measurements for three side element configurations, covering the Reynolds number representative of the scaled wind tunnel CFD simulations, with airspeed variations adjusted according to the instantaneous temperature during testing. Each test consisted of steady state force acquisition combined with local pressure mapping on the main wing of the side elements, as well as qualitative flow visualization using wool tufts to identify regions of flow attachment and separation.

Figure 8: Aeronautical wind tunnel at LNEC.

5. Wind Tunnel Testing and Comparison with CFD Simulations

The experimental and numerical results obtained for the three side element configurations of the FST14, designated as configurations A, B, and C, are presented and analyzed.

5.1. Formula Student Scaled Model

The 1:3 scale model of the FST14 used during the wind tunnel campaign represented the complete vehicle, as illustrated in Figure 9, and incorporated modular components such as the different side element assemblies analyzed.

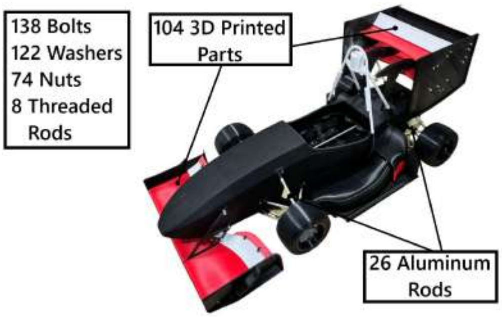

Figure 9: Final FST14 model.

The model was designed to maintain geometric fidelity across all external surfaces while providing sufficient structural stiffness to prevent deformation under loading. Mounting interfaces were integrated within the chassis interior to enable repeatable installation on the aerodynamic force balance, avoiding geometric misalignment and minimizing interference with the underfloor flow.

The wind tunnel airspeed was set to match the Reynolds number of the conditions simulated numerically for the 1:3 scale representation of the wind tunnel case, which was conducted under Standard Sea Level (SSL) conditions. The selected scale offered an optimal balance between manufacturing feasibility, aerodynamic representativeness, and compatibility with the test section, as shown in Figure 10. The same car geometry, including identical simplifications, was used in the CFD simulations to ensure consistency.

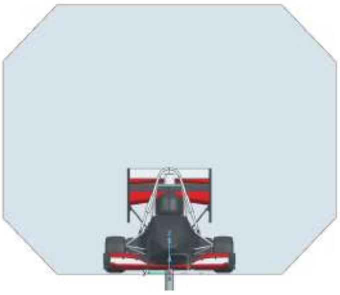

Figure 10: Scaled FS model inside the WT test section (frontal view).

5.2. Comparison of Pressure Distributions on the Side Diffuser

Surface pressures were recorded along chordwise and spanwise locations on the upper and lower surfaces of the main side wing. Figure 11 presents the experimental and numerical pressure coefficient distributions for configuration A, considered as the baseline case, together with additional modified numerical simulations. The data reveals strong agreement on the upper surface, where CFD accurately captured the suction region downstream of the stagnation point and the subsequent pressure recovery. On the lower surface, the discrepancies were considerably more noticeable, as the experimental results exhibited weaker suction peaks located further downstream. This deviation may be attributed to attitude changes observed during testing, as complementary simulations demonstrated that an increase in ride height leads to suction peak attenuation, while the downstream displacement of the minimum C_p was reproduced in a pitched angle simulation, confirming the sensitivity of the pressure distribution to variations in model attitude.

To further evaluate the influence of dynamic attitude changes on the results, the experimental trends between configurations A and B were compared with the numerical simulations at the nominal neutral attitude, as well as with the cases of increased ride height and nose-up pitch variation in Figure 12.

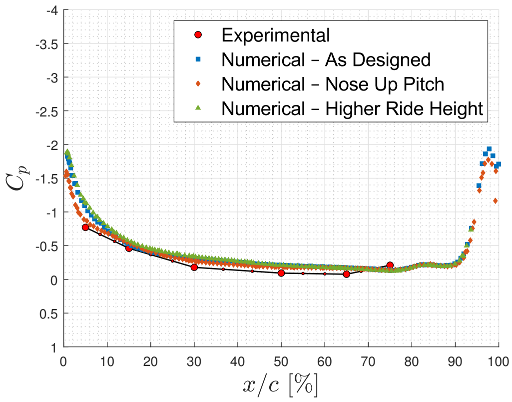

(a) Upper surface at $|y_2|/(w/2) = 49\%$.

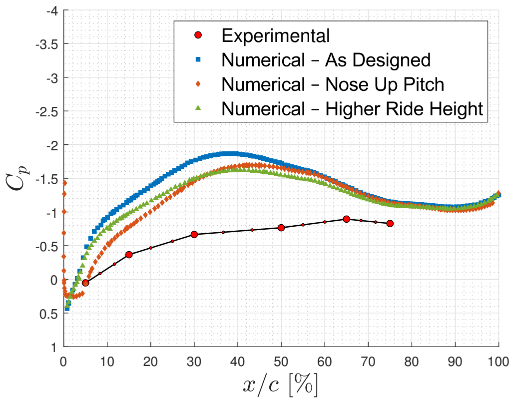

(b) Lower surface at $|y_2|/(w/2) = 49\%$.

Figure 11: Pressure distributions obtained experimentally and numerically for configuration A.

The analysis revealed that variations in the aerodynamic coefficients across these conditions remained below 15%, while indicating that the overall aerodynamic trends were preserved within an acceptable range. The main sensitivity was observed in the aerodynamic balance, which shifted under pitch variation due to the corresponding change in the longitudinal position of the pressure center, which is a direct impact of the rotation itself. Overall, the consistency between the numerical and experimental results confirmed the robustness of the as-designed numerical setup as a reliable baseline while highlighting the importance of considering realistic platform variations when comparing with experimental data.

5.3. Comparison of Aerodynamic Coefficients

The comparison of aerodynamic coefficients across the three side element configurations, summarized in Figure 13, shows agreement between numerical and experimental trends. From configuration A to B, both datasets indicate a clear increase in downforce accompanied by a moderate drag rise, confirming that the design modifications enhance

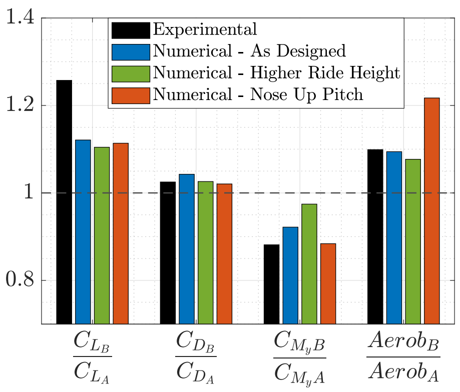

Figure 12: Sensitivity of aerodynamic coefficients of configuration B relative to configuration A with ride height and pitch angle.

load generation under WT conditions. Configuration C yields a slight reduction in downforce relative to B while maintaining higher performance than the baseline, together with a partial recovery in drag.

Overall, the consistency of trends between datasets indicates that the numerical setup is a reliable tool for comparative assessment of aerodynamic configurations. Despite differences in absolute magnitudes, the simulations accurately capture the relative aerodynamic behavior observed experimentally, supporting their use for subsequent aerodynamic analyses.

5.4. Flow Visualization

Wool tuft visualization was employed to complement the force and pressure measurements and qualitatively assess the flow behavior around the FST14. Tufts were attached to the right side of the 1:3 scale car model, and the flow was recorded simultaneously with the aerodynamic measurements. The experimental observations were compared with the limiting surface streamline plots and the skin friction coefficient, C_{f_x}, where positive values denote attached flow and negative values indicate separation.

The comparison between experimental and numerical results showed good overall agreement across the main aerodynamic components, particularly on the side elements. On the main side wing, both approaches identified predominantly attached flow near the inboard leading edge and localized separation toward the outboard region, mainly for configuration A, consistent with the numerical predictions shown in Figure 14. The presence of attached flow above the tubular vortex generator and separation over the footplate surface were accurately captured, while configuration C exhibited a noticeable reduction in flow separation compared to A. Downstream, the experimental wool tuft visualization and CFD streamlines also showed strong correspondence, consistently reproducing the flow structures generated by the side assembly with good agreement.

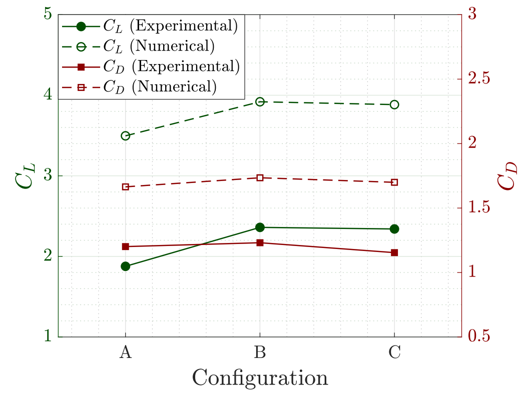

(a) Absolute values.

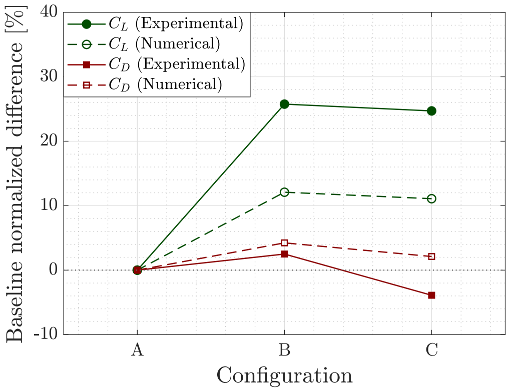

(b) Normalized values.

Figure 13: Lift and drag for the three tested configurations.

When comparing configurations, configuration A exhibited pronounced separation on the main and midplate leading edges and along the footplate, whereas configurations B and C effectively suppressed large scale detachment, promoting more coherent surface flow structures. This evolution reflects a clear aerodynamic improvement and confirms the design advantage of the later configurations.

Flow visualization of other components, including the front and rear wings, also showed satisfactory agreement between CFD and experiments. On the front wing, some discrepancies were observed: although attached flow along the main element was successfully captured on both ends, localized separation near the endplate was detected experimentally but not reproduced numerically. Tuft vibration confirmed that the incoming flow was already turbulent upon reaching the model, supporting the decision to omit a transition model in the simulations. At the rear wing, both approaches cap-

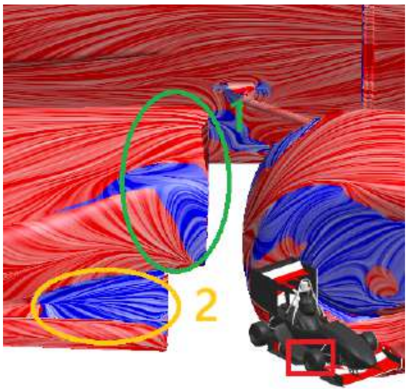

(a) CFD.

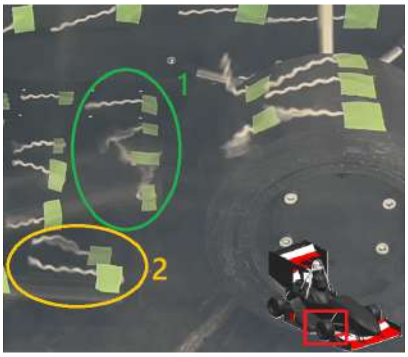

(b) EFD.

Figure 14: Flow visualization on main wing leading edge upper surface of configuration A.

tured endplate leading edge and flap separation regions, though small discrepancies appeared in local attachment on the upper sections. These differences highlight the local sensitivity of the flow in this area.

Overall, the tuft visualization results corroborate the fact that the CFD setup accurately reproduces the main flow features observed experimentally. Together with the force and pressure correlations presented previously, these findings establish confidence in the numerical methodology, providing a robust basis for subsequent on-track aerodynamic analysis.

6. Numerical Assessment of Differences between WT and On-Track Conditions

The main discrepancies between the WT setup and actual on-track operation are discussed in terms of their impact on aerodynamic performance. The parameters assessed numerically are ride height, Reynolds number related to the scaling, ground and wheel motion, and domain size.

6.1. Ride Height

As a first step, the model ground clearance was reduced from 5mm to 0mm across all configurations. The bottom view pressure field for configuration C (Figure 15) shows intensified suction beneath the floor and main side wing, with higher mass flow acceleration. The integrated coefficients in Figures 19a and 19b confirm a consistent rise in C_L for all configurations, while drag increases only marginally, maintaining the same performance trends. The aerobalance shifts modestly forward due to enhanced suction near the floor throat and front wing. The performance trends among configurations is preserved, and downforce generated by the side elements increases by about 10–15 %.

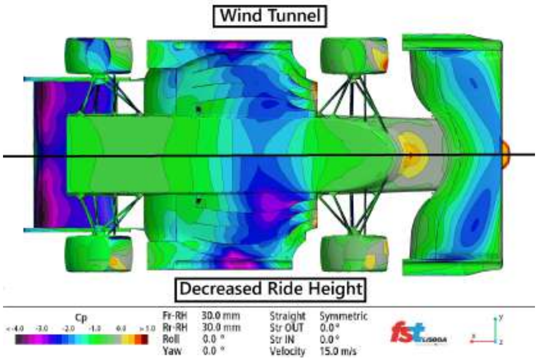

Figure 15: Ride height effect on pressure coefficient on model bottom for configuration C.

6.2. Reynolds Number

The second step restored fluid properties to full scale values, isolating Reynolds number effects. Surface static pressure coefficient on the bottom of the model show a deeper, more continuous low pressure footprint with sharper throat gradients, consistent with thinner boundary layers and reduced viscous diffusion. The coefficients indicate steeper increase in C_L with nearly constant C_D. Side element downforce increases for all configurations, with configuration B retaining the highest load. The aerobalance shifts forward, suggesting a more even distribution of Reynolds number effects between axles. The results also indicate that the variations primarily cause an almost uniform shift in the magnitude of the key aerodynamic parameters across configurations. Therefore, the relative trends established under wind tunnel conditions remain consistent so far, as illustrated in Figure 16, which shows that the normalized differences of the main coefficients relative to configuration A are largely preserved.

6.3. Moving Ground and Wheel Rotation

The next step introduced moving ground and rotating wheels. The ground speed matches free stream velocity and each wheel rotates at the correspondent angular speed (Figure 17).

The pressure distribution beneath the floor and side elements show pronounced suction, with stronger minima on the main wing and along the floor edge vortex generators. Eliminating the upstream floor boundary layer allows an almost uni-

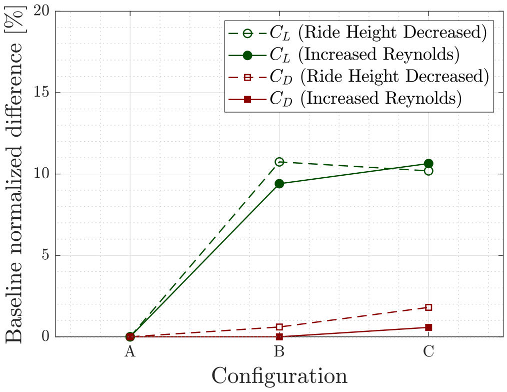

Figure 16: Influence of Reynolds number on normalized lift and drag coefficients for the tested configurations.

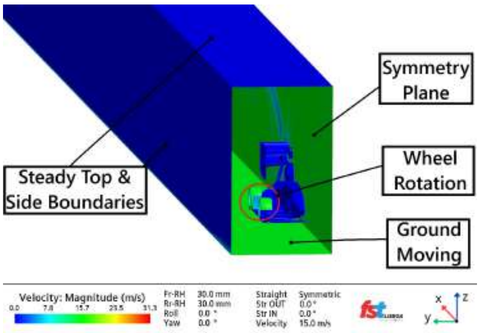

Figure 17: Boundary conditions with ground and wheels motion.

form approach flow and reinforces underfloor suction, as shown in Figure 18. The integrated response (Figures 19a and 19b) confirms higher C_L across all configurations, with the hierarchy $C_{L_C} > C_{L_B} > C_{L_A}$ now pronounced and exceeding numerical uncertainty for comparing configurations B and C. Drag exhibits configuration dependent behavior: configuration C increases due to higher underfloor mass flow and stronger vorticity, while configurations A and B remain neutral or slightly lower with smoother recovery limits induced and less vortex related losses. The aerodynamic balance shifts modestly forward, consistent with intensified front wing suction and a more momentum filled underbody stream. Introducing moving ground and rotating wheels before domain enlargement allowed to isolate blockage effects in the subsequent step by removing the confounding influence of the upstream floor boundary layer.

6.4. Domain Size

Finally, the computational domain was enlarged, in this case to a 7 × 10m cross section for the half-car simulation with lateral and top boundaries now set as symmetry planes, the inlet is moved to approximately 3 car lengths and the outlet is kept to 13 car lengths. The pressure distribution shows weaker suction under the floor and side elements, with smoother gradients, confirming that part of the previous load amplification arose from blockage effect. Figures 19a and 19b show decreases in both C_L and C_D for all configurations, reflecting reduced blockage. Downforce generated by the modified components drops as side vortices weaken without wall proximity. The aerobalance shifts mildly forward since the rear loses proportionally more load. Under the on-track domain, a clear hierarchy is observed: $C_{L_C} > C_{L_B} > C_{L_A}$, and for side element downforce, $DF_C > DF_B > DF_A$, accompanied by a more front-biased aerodynamic balance compared to the moving ground case. Configuration C benefits the most from realistic kinematics due to its underfloor and side element design. Configuration B remains competitive but exhibits greater sensitivity to operating conditions in terms of aerodynamic performance. Configuration A exhibits the lowest overall performance, serving primarily as a baseline reference for comparison.

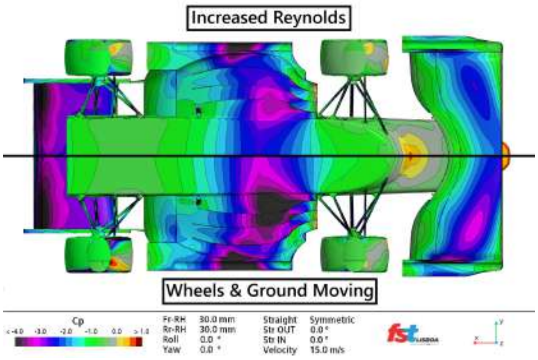

Figure 18: Influence of ground and wheel motion on pressure coefficient on model bottom for configuration C.

6.5. Geometry Comparison under On-Track Conditions

In summary, from the initial wind tunnel setup to the final on-track condition, a consistent increase in aerodynamic forces is observed, indicating that the progressive introduction of more realistic boundary conditions enhances overall load generation up to the stage where the domain size is expanded in the on-track simulations, as displayed in Figure 19. These findings confirm that the aerodynamic performance trends obtained under wind tunnel conditions differ significantly from those observed in on-track operation, preventing direct comparison without appropriate numerical corrections.

A comparison of configurations under the final on-track setup confirms the field level mechanisms. For configuration C, the bottom view C_p distribu-

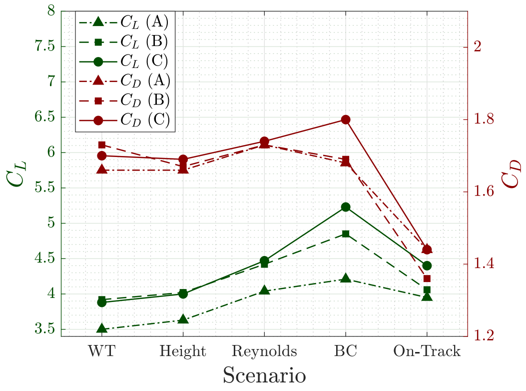

(a) Lift and drag coefficients.

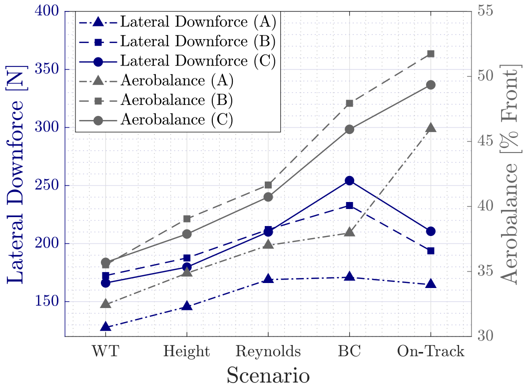

(b) Side elements' downforce and aerobalance.

Figure 19: Key aerodynamic parameters for the configurations across the simulated scenarios.

tion, illustrated in Figure 20 shows a broader and more upstream suction footprint on the main wing relative to configuration A, while front and rear wing load levels remain comparable. A total pressure coefficient analysis, C_{p_T}, suggest that the extended strakes in configuration C form compact vortex cores confined by the channel-like geometry, delaying breakdown and directing total pressure more efficiently beneath the side wing.

The integrated results in Table 1 quantify the differences among configurations: C_L increases from 3.95 (A) to 4.40 (C), C_D remains essentially unchanged at 1.44, and efficiency improves from $C_L/C_D = 2.74$ to 3.05 (+11.3 %). Aerobalance shifts forward from 45.98 % to 49.35 %. Downforce generated by the lateral components rises from 164.7 N to 210.6 N (+27.9 %). Mesh convergence estimates from Section 3 confirm that the gains from configuration A to C lie beyond numerical uncertainty, while the near equality in C_D aligns with the small drag uncertainty.

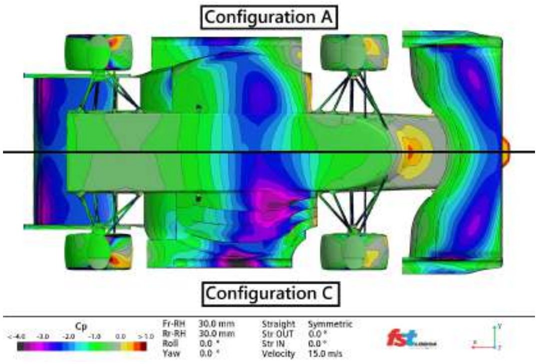

Figure 20: Comparison of pressure coefficient on model bottom for configurations C and A.

Table 1: Comparison of key aerodynamic parameters under on-track conditions.

Configuration	C_L	C_D	C_L/C_D	Aerobalance (% Front)	Lat. DF (N)
A	3.95	1.44	2.74	45.98	164.68
B	4.06	1.36	2.98	51.74	193.80
C	4.40	1.44	3.05	49.35	210.62

7. Conclusions

The present work developed, tested, and applied a computational and experimental framework for the aerodynamic design of the FST14. A complete 1:3 scale model was designed, manufactured, and tested at LNEC, reinstating WT experimentation as a reliable tool within the team's workflow. The numerical methodology was verified through a detailed mesh convergence study, establishing numerical errors of approximately ≈ 4.3% in C_L, ≈ 1.1% in C_D, and ≈ 3.2% in side element downforce.

The experimental phase involved calibrating the six-component balance, performing force and pressure measurements, and conducting tuft based flow visualization. The CFD simulations reliably reproduced the experimental trends, while discrepancies on the lower surfaces were attributed mainly to attitude variations during testing. The qualitative agreement of the flow visualization patterns with the numerical streamlines further reinforced the credibility of the numerical approach.

The CFD setup was then extended to simulate on-track conditions, progressively incorporating the effects of ride height, Reynolds number, ground and wheel motion, and flow confinement. This systematic approach isolated the impact of each parameter and demonstrated that configuration C delivered the highest aerodynamic efficiency and flow coherence under more realistic conditions. Relative to configuration A, configuration C achieved 11.4% increase in C_L, maintained C_D nearly constant, improved C_L/C_D by 11%, shifted the aerodynamic balance forward by 3.4%, and the specific side element downforce generated increased by 28%.

Although the main objectives were fulfilled, several areas remain open for further improvement. Experimentally, future campaigns should focus on increasing measurement precision and repeatability by refining the balance design, expand pressure tap network, and optimize calibration procedure. Implementing a moving ground and rotating wheels would better replicate on-track conditions, while additional visualization techniques, such as smoke or oil-flow methods, could provide deeper insight into three-dimensional flow behavior.

Numerically, future work should aim to reduce numerical uncertainty through targeted local mesh refinement in regions of steep pressure gradients and intense vorticity. The adoption of transitional or hybrid RANS–LES turbulence models could further improve simulation accuracy if computational resources allow.

References

[1] J. Katz. Aerodynamics in motorsports. *Proceedings of the Institution of Mechanical Engineers, Part P: Journal of Sports Engineering and Technology*, 235:175433711989322, December 2019. doi:10.1177/1754337119893226.

[2] W. Milliken and D. Milliken. *Race Car Vehicle Dynamics*. SAE International, 1994. ISBN 978-1560915263.

[3] O. Ehirim, K. Knowles, and A. Saddington. A review of ground-effect diffuser aerodynamics. *Journal of Fluids Engineering*, 141:020801, June 2018. doi:10.1115/1.4040501.

[4] Formula Student Germany. Rules for FSG 2025. https://www.formulastudent.de/fsg/rules/, 2024. Accessed on October 14, 2025.

[5] S. McBeath. *Competition Car Aerodynamics: A Practical Handbook - 3rd Edition*. Veloce Publishing Limited, 2017. ISBN 978-1787111028.

[6] Chen Fu, M. Uddin, C. Robinson, A. Guzman, and D. Bailey. Turbulence models and model closure coefficients sensitivity of NASCAR racecar RANS CFD aerodynamic predictions. *SAE International Journal of Passenger Cars - Mechanical Systems*, 10:330–344, March 2017. doi:10.4271/2017-01-1547.

[7] J. Anderson. *Fundamentals of Aerodynamics*. McGraw-Hill Series in Aeronautical and Aerospace Engineering, 2017. ISBN 978-1259129919.

[8] V. Brederode. *Aerodinâmica Incompressível: Fundamentos*. IST Press, 2014. ISBN 978-9898481320.

[9] J. Pacheco. Wind tunnel testing of a complete formula student vehicle. Master's thesis, Instituto Superior Técnico, Universidade de Lisboa, Portugal, 2022.

[10] L. Afonso. Aerodynamic design and wind tunnel testing of the rear end of a formula student vehicle. Master's thesis, Instituto Superior Técnico, Universidade de Lisboa, Portugal, 2022.

[11] J. Morgado. Design and testing of a rear wing for a formula student car. Master's thesis, Faculdade de Ciências - Universidade de Lisboa, Portugal, 2022.

[12] A. Oliveira. Design, construction, calibration and testing of a wind tunnel force balance. Master's thesis, Instituto Superior Técnico, Universidade de Lisboa, Portugal, 2020.

[13] Joseph Katz and Frederic Morey. Aerodynamics of large-scale vortex generator in ground effect. *Journal of Fluids Engineering*, 130, July 2008. doi:10.1115/1.2948361.

[14] X. Zhang, W. Toet, and J. Zerihan. Ground Effect Aerodynamics of Race Cars. *Applied Mechanics Reviews*, 59(1):33–49, 2006. doi:10.1115/1.2110263.

[15] Giancarlo Alfonsi. Reynolds-averaged navier-stokes equations for turbulence modeling. *Applied Mechanics Reviews*, 62, July 2009. doi:10.1115/1.3124648.

[16] F. Menter. Zonal two-equation κ–ω turbulence models for aerodynamic flows. In *23rd Fluid Dynamics, Plasmadynamics, and Lasers Conference*, Orlando, Florida, USA, 1993. American Institute of Aeronautics and Astronautics. doi:10.2514/6.1993-2906.

[17] L. Eça and M. Hoekstra. A procedure for the estimation of the numerical uncertainty of CFD calculations based on grid refinement studies. *Journal of Computational Physics*, 262:104–130, 2014. doi:10.1016/j.jcp.2014.01.006.

[18] L. Eça, G. Vaz, S. Toxopeus, and M. Hoekstra. Numerical errors in unsteady flow simulations. *Journal of Verification, Validation and Uncertainty Quantification*, 4, May 2019. doi:10.1115/1.4043975.

[19] M. Ferreira. Design of a six-component external wind tunnel balance. Master's thesis, Instituto Superior Técnico, Universidade de Lisboa, Portugal, 2015.